Finite volume discretization for poroelastic media with fractures modeled by contact mechanics

Runar L. Berge[1] | Inga Berre[1,2] | Eirik Keilegavlen[1] | Jan M. Nordbotten[1] | Barbara Wohlmuth[3]

[1]Department of Mathematics, University of Bergen, Norway

[2]NORCE, Norway

[3]Department of Mathematics, Technische Universität München, Germany

Correspondence
Runar L. Berge, Universitetet i Bergen Matematisk institutt, Postboks 7803, 5020 Bergen, Norway. Email: runar.berge@uib.no

Summary

A fractured poroelastic body is considered where the opening of the fractures is governed by a nonpenetration law while slip is described by a Coulomb-type friction law. This physical model results in a nonlinear variational inequality problem. The variational inequality is rewritten as a complementary function, and a semismooth Newton method is used to solve the system of equations. For the discretization, we use a hybrid scheme where the displacements are given in terms of degrees of freedom per element, and an additional Lagrange multiplier representing the traction is added on the fracture faces. The novelty of our method comes from combining the Lagrange multiplier from the hybrid scheme with a finite volume discretization of the poroelastic Biot equation, which allows us to directly impose the inequality constraints on each subface. The convergence of the method is studied for several challenging geometries in 2d and 3d, showing that the convergence rates of the finite volume scheme do not deteriorate when it is coupled to the Lagrange multipliers. Our method is especially attractive for the poroelastic problem because it allows for a straightforward coupling between the matrix deformation, contact conditions, and fluid pressure.

KEYWORDS:
Contact mechanics, Biot, fractures, finite volume

1 | INTRODUCTION

Slip and opening of fractures due to fluid injection is of relevance to a number of subsurface engineering processes. In hydraulic reservoir stimulation, the effect is deliberately induced, while in storage operations and wastewater disposal, avoiding reactivation and opening of fractures is important for preserving caprock integrity. In any circumstance, triggering of larger slip events in the form of elevated levels of seismicity must be avoided. The mathematical model of fracture resistance, slip and opening results in a strongly coupled nonlinear variational inequality, which requires advanced numerical schemes to solve. The purpose of this work is to describe and implement a numerical method to solve this problem considering a poroelastic matrix. The fractures are a set of predefined surfaces in the domain, and the nucleation or growth of fractures is not considered.

The flow and mechanics of poroelastic media and the contact mechanics of elastic bodies are well-developed research fields. For a porous or poroelastic medium, we refer to the classical textbooks[1,2]. There exists an extensive number of discretizations for the elliptic equations describing fluid flow in a porous medium, and they all have different merits. The most popular discretizations are the so-called locally conservative discretizations[3], which include mixed finite elements[4], control-volume

finite elements[5], and finite volume methods[6]. For the coupled poroelastic problem, without considering fractures, it is known that a naive discretization of the coupling terms of the fluid pressure and the solid displacement leads to stability issues for finite element schemes[7]. Several different methods have been proposed to remove these oscillations[8,9,10]. Recently, a finite volume method called the multipoint stress approximation was introduced for elastic deformations[11,12]. This method has been extended to the poroelastic Biot equations and shown to be stable without adding any artificial stabilization terms in the limit of incompressible fluids and small time steps[13].

The contact mechanics problem, i.e., contact between two elastic bodies, is also the topic of several textbooks[14,15]. A widely used solution strategy for the nonlinear variational inequalities resulting from the mathematical formulation is the penalty method[16]. The basic idea is to penalize a violation of the inequality by adding extra energy to the system. The solution depends then, in a very sensitive way, on the choice of the penalty parameter. If the value of the parameter is too small, the condition number of the algebraic system is extremely poor, and the nonlinear solver converges slowly. If the value is too large, the accuracy of the solution is very poor, and unphysical approximations can be obtained. Therefore, variationally consistent hybrid formulations have gained interest recently. The hybrid formulations are based on the discretization of additional unknown Lagrange multipliers added to the contact region. This method has been applied to, among others, the Signorini problem[17], frictional contact[18], and large deformations[19]; see the survey contribution[20] and the references therein.

For a poroelastic domain including fractures, different models for the contact problem are developed[21,22,23,24]. Most of these models, however, do not take into account the contact problem either by assuming the fractures stick together[21] or that the fluid pressure inside the fractures is so large that the fracture surfaces are never in contact[22,23]. The full contact problem for a fractured poroelastic domain is considered by Garipov et al[24], where they applied the penalty method to solve the nonlinear variational inequalities resulting from the contact problem.

In the current work, we present a different numerical solution approach for poroelastic media with contact mechanics. The discretization is based on a finite volume method for poroelasticity[13] combined with a variationally consistent hybrid discretization[25,20]. The hybrid formulation considered in this work can be regarded as a mortar formulation[26] using matching meshes with the displacement as the primal variable and the surface traction as the dual variable. The finite volume scheme has previously been extended to fracture deformation by adding additional displacement unknowns on the fracture faces[27]. This formulation was successfully used to implement a fixed-point type iteration to approximate the friction bound[28]; however, this formulation suffers from the fact that a step length parameter needs to be tuned and that it might require many iterations to converge[29]. An advantage of the scheme used in this work, where the Lagrange multiplier of the hybrid formulation is coupled with the surface traction obtained from the finite volume scheme, is that it gives a natural formulation of the contact condition per subface. This formulation allows us to rapidly solve the resulting nonlinear inequality problem by applying a semismooth Newton method; see the work by Hüeber et al[25], among others[20,30].

The remainder of this paper is structured as follows. First, we state the problem and give the governing equations. Then, the discretization is presented, which is divided into two parts: (i) the finite volume discretization for the Biot equations and (ii) the discrete hybrid formulation for the contact problem. We present four numerical examples. The first two consider the dry case where the coupling between fluid pressure and deformation of the rock is disregarded. The last two examples solves the poroelastic deformation of a 2d and 3d domain where the deformation of fractures is governed by a Coulomb friction law. Finally, we give concluding remarks.

2 | PROBLEM STATEMENT

Let Ω be a fractured deformable porous body. The boundaries of the domain $\partial\Omega$ are divided into three disjoint open sets, Γ_D, Γ_N, and Γ_C, as illustrated in Figure 1: for the first set, a Dirichlet boundary condition is assigned; for the second, a Neumann boundary condition is assigned; and the last is the internal fracture boundary. We consider the Biot model for a poroelastic
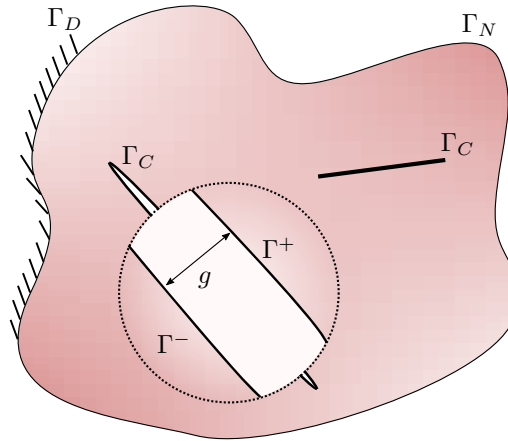
FIGURE 1 A domain Ω where the external boundary is divided into two parts: Γ_D and Γ_N. Included in the domain are two internal boundaries, or fractures, Γ_C. The two sides of the internal boundaries are labeled Γ^+ and Γ^-, as shown in the magnified circular region of the domain. The function $g(\boldsymbol{x}), \boldsymbol{x} \in \Gamma^+$ gives the initial gap between the two fracture sides. The left fracture has an initial gap $g > 0$, while the top right fracture has an initial gap $g = 0$.

medium[31]:

$$
\begin{aligned}
-\nabla \cdot \sigma &= \boldsymbol{f}_u & &\text{in } \Omega, \\
C : (\nabla \boldsymbol{u} + (\nabla \boldsymbol{u})^\top)/2 - \alpha p I &= \sigma & &\text{in } \Omega, \\
c_0 \dot{p} + \alpha \nabla \cdot \dot{\boldsymbol{u}} + \nabla \cdot \boldsymbol{q} &= f_p & &\text{in } \Omega, \\
\boldsymbol{q} &= -\mathcal{K} \nabla p & &\text{in } \Omega, \\
\boldsymbol{u} &= \boldsymbol{g}_{u,D} & &\text{on } \Gamma_{u,D}, \\
\sigma \cdot \boldsymbol{n} &= \boldsymbol{g}_{u,N} & &\text{on } \Gamma_{u,N}, \\
p &= g_{p,D} & &\text{on } \Gamma_{p,D}, \\
\boldsymbol{q} \cdot \boldsymbol{n} &= g_{p,N} & &\text{on } \Gamma_{p,N}.
\end{aligned}
\tag{1}
$$

The variables $\dot{p}$ and $\dot{\boldsymbol{u}}$ are the time derivatives of the pressure and displacement, respectively. Throughout this paper we apply a backward Euler time stepping, and $\dot{p}$ and $\dot{\boldsymbol{u}}$ should be interpreted as the discrete derivatives

$$
\dot{p} = \frac{p - p^i}{\Delta t}, \quad \dot{\boldsymbol{u}} = \frac{\boldsymbol{u} - \boldsymbol{u}^i}{\Delta t},
\tag{2}
$$

for the previous time iterate i and time step length Δt. Note that we have dropped the index for the current time iterate, $i + 1$. All parameters are, in general, functions of space, e.g., $C = C(\boldsymbol{x})$, $\boldsymbol{x} \in \Omega$; however, the explicit dependence is suppressed to keep the notation simple. Parameters associated with the pressure p and displacement $\boldsymbol{u}$ are given a subscript with the same symbol. The vector $\boldsymbol{f}_u$ is a given body force, while f_p is a given source term. The stiffness tensor is denoted C, the Biot coupling coefficient α, the storage coefficient c_0, and the permeability $\mathcal{K}$. Indicated by subscripts, $\boldsymbol{g}$ represents Dirichlet and Neumann boundary conditions for displacement and pressure, while $\boldsymbol{n}$ is the outwards pointing normal vector. In this work, we use $C : (\nabla \boldsymbol{u} + (\nabla \boldsymbol{u})^\top)/2 = G(\nabla \boldsymbol{u} + (\nabla \boldsymbol{u})^\top) + \Lambda \mathrm{tr}(\nabla \boldsymbol{u}) I$, where G and Λ are the Lamé parameters. Traction can also be derived for other material laws.

The fracture boundary, Γ_C, is divided into a positive side Γ^+ and a negative side Γ^+. The choice of which side is positive and which is negative is arbitrary and will only make a difference in the implementation. For the fracture segments, a nonpenetration condition is enforced in the normal direction, meaning that the positive and negative sides cannot penetrate each other. In the tangential direction, a Coulomb friction law divides the contact region into a sliding part and a sticking part. To formulate these contact conditions, the normal vector for the contact region is defined as the normal vector of the positive side $\boldsymbol{n}(\boldsymbol{x}) = \boldsymbol{n}^+(\boldsymbol{x})$. Further, let

$$
R : \Gamma^+ \to \Gamma^-
\tag{3}
$$

be a mapping that projects a point from the positive boundary onto the negative boundary as given by the normal vector. The gap function, which will appear in the nonpenetration condition, is then defined as

$$g(x) = \|x - R(x)\| \quad x \in \Gamma^+,$$

where $\|\cdot\|$ is the Euclidean norm. Due to Newton's third law, the surface traction, $T = \sigma \cdot n$, on the contact boundaries must be equal up to the sign

$$T^+(x) = -T^-(R(x)) \qquad x \in \Gamma^+, \tag{4}$$

and we use the notation $T_C = T^+$. The surface traction is divided into a normal and tangential part by

$$T_n(x) = T_C(x) \cdot n(x), \quad T_\tau(x) = T_C(x) - T_n(x)n(x) \qquad x \in \Gamma^+, \tag{5}$$

and the displacement jump is defined as $[u(x)] = u(x) - u(R(x))$ for $x \in \Gamma^+$. The normal and tangential displacement jump is defined analogously to Equation (5):

$$[u(x)]_n = [u(x)] \cdot n(x), \quad [u(x)]_\tau = [u(x)] - [u(x)]_n n(x) \qquad x \in \Gamma^+.$$

The nonpenetration condition can now be formulated as

$$\begin{cases} [u(x)]_n - g(x) \leq 0 \\ T_n(x)([u(x)]_n - g(x)) = 0 \qquad x \in \Gamma^+, \\ T_n(x) \leq 0 \end{cases} \tag{6}$$

where the first condition ensures that the two sides of the fracture cannot penetrate, the second ensures that either the normal traction is zero or the fracture sides are in contact, and the last enforces a negative normal component of the surface traction.

The tangential part of the surface traction is governed by a Coulomb friction law:

$$\begin{cases} \|T_\tau(x)\| \leq F(x)|T_n(x)| \\ \|T_\tau(x)\| < F(x)|T_n(x)| \to [\dot{u}(x)]_\tau = 0 \qquad x \in \Gamma^+, \\ \|T_\tau(x)\| = F(x)|T_n(x)| \to \exists \zeta \in \mathbb{R} : T_\tau(x) = -\zeta^2[\dot{u}(x)]_\tau \end{cases} \tag{7}$$

where F is the coefficient of friction, and $\dot{u}$ is the displacement velocity approximated by the backward Euler scheme, as given by Equation (2). The first equation gives the friction bound, the second ensures that if the friction bound is not reached, then the surface is sticking, and the last equation ensures that if the friction bound is reached, then the tangential sliding velocity is parallel to the tangential traction. In the static case, e.g., for the purely mechanical problem when $\alpha = 0$, the notion of a velocity does not exist. For these cases, it is common to replace the sliding velocity, $[\dot{u}]_\tau$, by the displacement jump, $[u]_\tau$, in Equation (7)[20].

For the fluid, the fractures are modeled as impermeable. This means that the fluid cannot flow in or across the fractures, i.e., $q(x) \cdot n(x) = 0$, $x \in \Gamma_C$. To avoid excessive model complexity, we have chosen a model with impermeable fractures. For possible methods to extend this work to include fracture flow, we refer to the work by Dietrich et al[32], among others[33,24,34,35].

3 | DISCRETIZATION

We define the triplet $(\mathcal{T}, \mathcal{F}, \mathcal{V})$ as the cells, faces and vertices of our mesh. It is assumed that the mesh conforms to the fractures; that is, the positive and negative sides of the fractures are tessellated by a subset of the faces of the mesh. Before the discretization is described, we need to define some notation, and we start by giving the relation between cells, faces and vertices using the standard notation for finite-volume methods[36,13]:

- For a cell $K \in \mathcal{T}$, we denote its faces by $\mathcal{F}_K$ and its vertices by $\mathcal{V}_K$.

- For a face $\pi \in \mathcal{F}$, we denote the neighboring cells as $\mathcal{T}_\pi$ and its vertices as $\mathcal{V}_\pi$.

- For a vertex $v \in \mathcal{V}$, we denote the adjacent cells by $\mathcal{T}_v$ and the adjacent faces by $\mathcal{F}_v$.

In addition to the mesh triplet $(\mathcal{T}, \mathcal{F}, \mathcal{V})$, we define the so-called subcells and subfaces illustrated in Figure 2:

- For a vertex $v \in \mathcal{V}_K$, we define a subcell of K identified by (K, v) with a volume m_K^v such that $\sum_{v \in \mathcal{V}_K} m_K^v = m_K = \int_K dx$.

- For a vertex $v \in \mathcal{V}_\pi$, we associate a subface identified by (π, v) with an area m_π^v such that $\sum_{v \in \mathcal{V}_\pi} m_\pi^v = m_\pi = \int_\pi dx$.
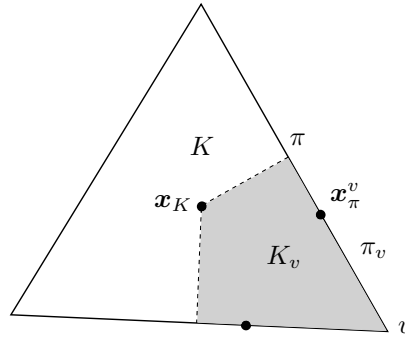
FIGURE 2 Notation used to describe the mesh. For a cell K, face π and vertex v of the mesh, we associate a subcell (K, v) and subface (π, v), as well as a cell center $\boldsymbol{x}_K$ and continuity point $\boldsymbol{x}_\pi^v$. In this figure, the cell is the full triangle, and the subcell is given by the gray area.

The subfaces cannot be chosen arbitrary but should correspond to faces of the subcells; for the triplet (v, π, K), the intersection of the boundary of the subcell (K, v) and the face π should equal the subface $(\pi, v) = \partial(K, v) \cap \pi$. Further, all subcells and subfaces are assumed to have a positive measure. Note that in an abuse of notation, we use K for both indexing and the geometric object so that both $\mathcal{V}_K$ and $\int_K \mathrm{d}\boldsymbol{x}$ make sense. All subfaces (π, v), $\pi \in \mathcal{F}$, $v \in \mathcal{V}_\pi$ are divided into three disjoint sets $\mathcal{P}, \mathcal{N}$, and $\mathcal{R}$, where $\mathcal{P}$ contains all subfaces located on the positive boundary Γ^+, $\mathcal{N}$ contains all subfaces located on the negative boundary Γ^-, and $\mathcal{R}$ contains the remaining subfaces.

Finally, for each element $K \in \mathcal{T}$, a cell center $\boldsymbol{x}_K \in K$ is defined, and for each subface (π, v), we associate a continuity point $\boldsymbol{x}_\pi^v$ located at any point on the subface, (π, v), however, the distance to the vertex v must be greater than zero. The unit normal for each face is denoted by $\boldsymbol{n}_\pi$, which is equal to the subface normal of the face $\boldsymbol{n}_\pi^v$. When it is necessary to distinguish the direction of the normal, it is defined as the outward pointing normal $\boldsymbol{n}_K^\pi$ of a cell $K \in \mathcal{T}_\pi$. Note that for a face π, we have $\mathcal{T}_\pi = \{K, L\}$, $\boldsymbol{n}_K^\pi = -\boldsymbol{n}_L^\pi$.

In the implementation used in the examples of this paper, the following construction is employed: The face- and cell-centers are chosen as the centroid of the corresponding face and cell. In 2d, the subface (π, v) is defined by the convex-hull of the vertex v and the face-center $\boldsymbol{x}_\pi$. In 3d, the subface is in addition defined by the midpoints of the edges of the face π that are connected to v. For simplices, this construction partition each face into a set of subfaces of equal area. The subcell (K, v) is defined by the convex-hull of the cell-center $\boldsymbol{x}_K$ and the subfaces (π, v), $\pi \in \mathcal{F}_v \cap \mathcal{F}_K$. The continuity point, $\boldsymbol{x}_\pi^v$, is taken to be one third the distance from the face-center to the vertex, $\boldsymbol{x}_\pi^v = \boldsymbol{x}_\pi - (\boldsymbol{x}_\pi - v)/3$. An example of this construction is shown in Figure 2.

3.1 | Finite volume discretization

We use a finite volume discretization [13] to discretize the Biot Equations (1). This is based on two discrete variables, $\boldsymbol{u}_K$ and p_K, which are the cell-centered displacement and pressure, respectively. Within each subcell (K, v), $K \in \mathcal{T}$, $v \in \mathcal{V}_K$, it is assumed that the displacements and pressures are linear in each subcell, and the discrete gradients are denoted by $(\bar{\nabla}\boldsymbol{u})_K^v$ and $(\bar{\nabla}p)_K^v$, where the bar over the gradient operator is added to distinguish it from the continuous gradients. For the mechanical stress, we adapt the notion of weak symmetry [12]; given the volume weighted average

$$\langle \Xi \rangle_v = \frac{1}{\sum_{K \in \mathcal{T}_v} m_K^v} \sum_{K \in \mathcal{T}_v} m_K^v \Xi_K^v,$$

associated with a vertex v, the discrete weakly symmetric mechanical stress is given by

$$\theta_K^v = C_K : (\bar{\nabla}\boldsymbol{u})_K^v - \frac{\langle C : (\bar{\nabla}\boldsymbol{u}) \rangle_v - \langle C : (\bar{\nabla}\boldsymbol{u}) \rangle_v^\top}{2}. \tag{8}$$

This is referred to as weak symmetry because

$$\langle \theta - \theta^\top \rangle_v = 0.$$

To simplify notation, the tensor C_K^v is referred to as the stress tensor, which acts to weakly symmetrize the stress:

$$\theta_K^v = C_K^v : (\bar{\nabla}\boldsymbol{u})_K^v.$$

The expression $C_K^v : (\bar{\nabla}\boldsymbol{u})_K^v$ should not be interpreted as a single tensor vector product but as a weighted sum of products given by Equation (8).

Using the weak symmetry, the flux and traction over each subface given by the discrete variables can be stated as

$$q_{K,\pi}^v = -m_\pi^v \mathcal{K}_K (\bar{\nabla}p)_K^v \cdot \boldsymbol{n}_K^\pi, \tag{9}$$

$$\boldsymbol{T}_{K,\pi}^v = m_\pi^v (C_K^v : (\bar{\nabla}\boldsymbol{u})_K^v - \alpha p_K I) \cdot \boldsymbol{n}_K^\pi. \tag{10}$$

For a spatially varying permeability and stress tensor, we use the cell-center value to evaluate the parameters $\mathcal{K}_K = \mathcal{K}(\boldsymbol{x}_K)$ for each cell.

The finite-volume scheme will be constructed such that the gradient unknowns can be eliminated by performing a local static condensation. The following presentation on how we obtain the numerical gradients is designed to reflect the computer implementation. This presentation is different from most classical papers on the used finite-volume discretization[6], however, it is mathematically equivalent. After the numerical gradients are expressed in terms of the cell-center unknowns, the finite volume structure of the discretization is obtained by enforcing mass/momentum conservation for each cell. The final scheme will be locally conservative and given by the cell-centered displacement and pressure. A detail that will be important when we introduce the hybrid discretization is the possibility of exactly reconstructing the discrete gradients, and thus also the flux and traction, from the cell-centered variables $\boldsymbol{u}$ and p.

The discrete fluid flux given in Equation (9) does not contain any dependence on the displacement, and it is identical to the fluid flux for the uncoupled fluid pressure, i.e., $\alpha = 0$. To discretize the flux, we use the MPFA-O scheme for simplices[37,38]. Each subcell gradient $(\bar{\nabla}p)_K^v$ is associated with a fluid flux as given in (9). Conservation of mass is enforced for each internal subface. This requires the fluid flux for cells $(K, L) \in \mathcal{T}_\pi$ sharing a face π to be equal and opposite over each of their shared subfaces; that is,

$$-m_\pi^v \mathcal{K}_K (\bar{\nabla}p)_K^v \cdot \boldsymbol{n}_K^\pi = m_\pi^v \mathcal{K}_L (\bar{\nabla}p)_L^v \cdot \boldsymbol{n}_L^\pi. \tag{11}$$

The pressure is not required to be continuous across the whole subface. Instead, pressure continuity is enforced at the continuity points, $\boldsymbol{x}_\pi^v$, that is,

$$p_K + (\bar{\nabla}p)_K^v \cdot (\boldsymbol{x}_\pi^v - \boldsymbol{x}_K) = p_L + (\bar{\nabla}p)_L^v \cdot (\boldsymbol{x}_\pi^v - \boldsymbol{x}_L). \tag{12}$$

Here, we have made use of the assumption that the pressure is linear in each subcell to write the pressure at the continuity point $\boldsymbol{x}_\pi^v$ as a function of the cell center pressure p_K and gradient $(\bar{\nabla}p)_K^v$. If a subface is on the Neumann boundary, $\pi \subset \Gamma_{p,N}$, the flux over the subface is given by evaluating the boundary condition at the continuity point and multiply the value with the subface area:

$$-m_\pi^v \mathcal{K}_K (\bar{\nabla}p)_K^v \cdot \boldsymbol{n}_K^\pi = m_\pi^v g_{p,N}(\boldsymbol{x}_\pi^v). \tag{13}$$

If a subface is on the Dirichlet boundary, $\pi \subset \Gamma_{p,D}$, the pressure on the subface is given by

$$p_K + (\bar{\nabla}p)_K^v \cdot (\boldsymbol{x}_\pi^v - \boldsymbol{x}_K) = g_{p,D}(\boldsymbol{x}_\pi^v). \tag{14}$$

Faces on the fracture boundary, $(\pi, v) \subset \Gamma^+ \cup \Gamma^-$, is given a zero Neumann boundary condition as we have assumed impermeable fractures.

Around each vertex v we can now form a local linear system of equations from which the gradients $(\bar{\nabla}p)_K^v$, $K \in \mathcal{T}_v$ can be eliminated:

$$(\bar{\boldsymbol{\nabla}}\boldsymbol{p})_v = \begin{bmatrix} Q_p \\ D_{p,G} \end{bmatrix}^{-1} \left(\begin{bmatrix} \boldsymbol{g}_{p,N} \\ \boldsymbol{g}_{p,D} \end{bmatrix} - \begin{bmatrix} 0 \\ D_p \end{bmatrix} \boldsymbol{p} \right). \tag{15}$$

The first block $Q_p(\bar{\boldsymbol{\nabla}}\boldsymbol{p})_v = \boldsymbol{g}_{p,N}$ in this linear system is the collection of all flux balance Equations (11) and (13) for the vertex v. The next block $D_{p,G}(\bar{\boldsymbol{\nabla}}\boldsymbol{p})_v = \boldsymbol{g}_{p,D} - D_p \boldsymbol{p}$ collects all the pressure continuity Equations (12) and (14). Thus, $(\bar{\boldsymbol{\nabla}}\boldsymbol{p})_v$ is the vector of the subcell gradients $(\bar{\nabla}p)_K^v$, the matrix Q_p represents products of the form $m_\pi^v \boldsymbol{n}_K^\pi \mathcal{K}_K$, the matrix $D_{p,G}$ represents the distances $\boldsymbol{x}_\pi^v - \boldsymbol{x}_K$, the vectors $\boldsymbol{g}_{p,N}$ and $\boldsymbol{g}_{p,D}$ are possible boundary conditions, and D_p has entries 1 for p_K^v and -1 for p_L^v.

The elimination of the displacement gradients $(\bar{\nabla}\boldsymbol{u})_K^v$ is similar to the elimination of the pressure gradients $\bar{\nabla}p_K^v$. First, the continuity of traction gives us for each internal subface

$$m_\pi^v (C_K^v : (\bar{\nabla}\boldsymbol{u})_K^v - \alpha p_K I) \cdot \boldsymbol{n}_K^\pi = -m_\pi^v (C_L^v : (\bar{\nabla}\boldsymbol{u})_L^v - \alpha p_L I) \cdot \boldsymbol{n}_L^\pi. \tag{16}$$

It is worth pointing out that, for internal faces, the averaging part of the operator $C_K^v : (\bar{\nabla}\boldsymbol{u})_K^v$ is the same on the right- and left-hand sides. Thus, the balance of traction can be written as

$$m_\pi^v (C_K : (\bar{\nabla}\boldsymbol{u})_K^v - \alpha p_K I) \cdot \boldsymbol{n}_K^\pi = -m_\pi^v (C_L : (\bar{\nabla}\boldsymbol{u})_L^v - \alpha p_L I) \cdot \boldsymbol{n}_L^\pi.$$

However, for boundary faces, the complete Equation (16) must be used. Unlike the fluid fluxes in (9), the traction is different from the uncoupled system due to the term $\alpha p_K I$. It is important to include the Biot stress in the local systems to obtain the correct force balance in our method[13]. We will see later that this approach also gives a higher-order term in the mass balance for the fluid, which acts analogously to the stabilization terms in other colocated schemes. For the fluid pressure, displacement continuity is enforced at the continuity points $\boldsymbol{x}_\pi^v$:

$$\boldsymbol{u}_K + (\bar{\nabla}\boldsymbol{u})_K^v(\boldsymbol{x}_\pi^v - \boldsymbol{x}_K) = \boldsymbol{u}_L + (\bar{\nabla}\boldsymbol{u})_L^v(\boldsymbol{x}_\pi^v - \boldsymbol{x}_L). \tag{17}$$

For a subface on the Neumann boundary, $(\pi, v) \subset \Gamma_{u,N}$, the boundary condition is evaluated at the continuity point and multiplied with the subface area:

$$m_\pi^v(C_K^v : (\bar{\nabla}\boldsymbol{u})_K^v - \alpha p_K I) \cdot \boldsymbol{n}_K^\pi = m_\pi^v \boldsymbol{g}_{u,N}(\boldsymbol{x}_\pi^v), \tag{18}$$

For a subface on the Dirichlet boundary $(\pi, v) \subset \Gamma_{u,D}$ the displacement vector at the continuity point is given:

$$\boldsymbol{u}_K + (\bar{\nabla}\boldsymbol{u})_K^v(\boldsymbol{x}_\pi^v - \boldsymbol{x}_K) = \boldsymbol{g}_{u,D}(\boldsymbol{x}_\pi^v). \tag{19}$$

Subfaces on the fracture boundary is given a Neumann condition defined by the Lagrange multiplier:

$$\begin{aligned} m_\pi^v(C_K^v : (\bar{\nabla}\boldsymbol{u})_K^v - \alpha p_K I) \cdot \boldsymbol{n}_K^\pi &= m_\pi^v \boldsymbol{\lambda}_\pi^v && (\pi, v) \in \mathcal{P}, \\ m_\pi^v(C_K^v : (\bar{\nabla}\boldsymbol{u})_K^v - \alpha p_K I) \cdot \boldsymbol{n}_K^\pi &= -m_\pi^v \boldsymbol{\lambda}(R^{-1}(\boldsymbol{x}_\pi^v)) && (\pi, v) \in \mathcal{N}. \end{aligned} \tag{20}$$

The contribution to the negative side $-\boldsymbol{\lambda}(R^{-1}(\boldsymbol{x}_\pi^v))$ is just the mapping onto the Lagrange multiplier on the corresponding positive subface as given by Equation (3).

A local elimination of the displacement gradients $(\bar{\nabla}\boldsymbol{u})_K^v$ can now be done around each vertex to express them in terms of the cell-center displacement and pressure:

$$(\bar{\boldsymbol{\nabla}}\boldsymbol{u})_v = \begin{bmatrix} Q_u \\ D_{u,G} \end{bmatrix}^{-1} \left(\begin{bmatrix} \boldsymbol{g}_{u,N} \\ \boldsymbol{g}_{u,D} \end{bmatrix} - \begin{bmatrix} P & 0 & -M_\pm \\ 0 & D_U & 0 \end{bmatrix} \begin{bmatrix} \boldsymbol{p} \\ \boldsymbol{u} \\ \boldsymbol{\lambda} \end{bmatrix} \right), \tag{21}$$

The variable $(\bar{\boldsymbol{\nabla}}\boldsymbol{u})_v$ is the vector of the displacement gradients, $(\bar{\nabla}\boldsymbol{u})_K^v$, around the vertex v, the matrix Q_u represents products of the form $m_\pi^v \boldsymbol{n}^\top C_K^v$, the matrix $D_{u,G}$ represents the same distance vectors as in (15), the vectors $\boldsymbol{g}_{u,N}$ and $\boldsymbol{g}_{u,D}$ are possible boundary conditions, and D_u is a matrix with entries ± 1. The term P is the only difference between the coupled and uncoupled system and contains products of the form $m_\pi^v \alpha I \boldsymbol{n}_\pi^v$, and the matrix $M_\pm$ contains the positive areas m_π^v for the positive subfaces and the negative areas $-m_\pi^v$ for the negative subfaces and represents the Lagrange multiplier contribution to the traction balance in Equation (20).

The finite-volume discretization of fluid flow is then obtained by expressing the fluid mass conservation over each cell K in terms of the discrete variables,

$$\sum_{\pi \in \mathcal{F}_K} \sum_{v \in \mathcal{V}_\pi} -m_\pi^v \mathcal{K}_K(\bar{\nabla}p)_K^v \cdot \boldsymbol{n}_K^\pi + \sum_{v \in \mathcal{V}_K} [m_K^v \alpha(\bar{\nabla} \cdot \dot{\boldsymbol{u}})_K^v + c_0 m_K^v \dot{p}_K] = \int_K f_p \, \mathrm{d}\boldsymbol{x}. \tag{22}$$

The pressure gradient $(\bar{\nabla}p)_K^v$ and displacement divergence $(\bar{\nabla} \cdot \boldsymbol{u})_K^v = \mathrm{tr}(\bar{\nabla}\boldsymbol{u})_K^v$ are obtained as linear functions of the cell-centered pressures and displacements and Lagrange multipliers from the local systems given in (15) and (21). The appearance of the pressure in the discrete displacement divergence is essential for the consistency of the method and is similar to the artificially introduced stability terms in other methods; see, e.g., Gaspar et al[39].

For the mechanics, momentum is conserved for all cells K,

$$-\sum_{\pi \in \mathcal{F}_K} \sum_{v \in \mathcal{V}_\pi} m_\pi^v C_K^v : (\bar{\nabla}\boldsymbol{u})_K^v \cdot \boldsymbol{n}_K^\pi = \int_K \boldsymbol{f} \, \mathrm{d}V. \tag{23}$$

Note that the term $\alpha p_K I$ from the Biot stress in (10) sums to zero over a cell due to Gauss's theorem; however, the pressure dependence on the subcell gradients gives the correct fluid pressure contribution to the mechanics. Similarly, the dependence of the Lagrange multiplier on the subcell gradients gives the correct force contribution to the momentum balance.

To summarize, the finite volume scheme is constructed by defining a set of discrete pressure and displacement gradients for each subcell. Flux and pressure continuity is enforced over each subface for the fluid, and traction and displacement continuity is enforced for each subface for the solid. This defines a small local system around each node from which the pressure and displacement gradients can be expressed as a linear combination of the cell-centered pressure and displacement, and Lagrange

multiplier and then eliminated. A stable coupling between the fluid and solid is achieved by considering the Biot stress, i.e., $C : (\nabla \boldsymbol{u} + (\nabla \boldsymbol{u})^\top)/2 - \alpha p I$, for traction balance of the local systems.

3.2 | Hybrid formulation

To solve the contact conditions (6) and (7), we apply the active-set strategy, which is equivalent to a semismooth Newton method described by Hüeber et al[25]. See also the paper by Wohlmuth[20]. We recapitulate the solution strategy in this section for the completeness of this paper. The main difference in our approach is how the Lagrange multipliers, which represent the surface traction, are coupled to the displacement unknowns in the surrounding domain. In our finite volume scheme, the Lagrange multipliers enter into the local equations for the displacement gradients.

A set of Lagrange multipliers is defined on the positive subface boundaries

$$\boldsymbol{\lambda}_\pi^v = \sigma_\pi^v \cdot \boldsymbol{n}_\pi^v, \qquad (\pi, v) \in \mathcal{P}.$$

The normal $\lambda_{\pi n}^v$ and tangential $\boldsymbol{\lambda}_{\pi\tau}^v$ components of the Lagrange multiplier are defined analogously to (5). The displacement on the subfaces, $\boldsymbol{u}_\pi^v$, is obtained as in Equation (19) for local systems.

The discrete formulation of the nonpenetration condition (6) can for each subface be written as

$$\begin{cases} [\boldsymbol{u}_\pi^v]_n - g_\pi^v \le 0 \\ \lambda_{\pi n}^v ([\boldsymbol{u}_\pi]_n^v - g_\pi^v) = 0 \qquad (\pi, v) \in \mathcal{P}, \\ \lambda_{\pi n}^v \le 0 \end{cases} \tag{24}$$

and the static Coulomb friction (7) as

$$\begin{cases} \|\boldsymbol{\lambda}_{\pi\tau}^v\| \le F_\pi^v |\lambda_{\pi n}^v| \\ \|\boldsymbol{\lambda}_{\pi\tau}^v\| < F_\pi^v |\lambda_{\pi n}^v| \to [\dot{\boldsymbol{u}}_\pi^v]_\tau = 0 \qquad (\pi, v) \in \mathcal{P}. \\ \|\boldsymbol{\lambda}_{\pi\tau}^v\| = F_\pi^v |\lambda_{\pi n}^v| \to \exists \zeta \in \mathbb{R} : \boldsymbol{\lambda}_{\pi\tau}^v = -\zeta^2 [\dot{\boldsymbol{u}}_\pi^v]_\tau \end{cases} \tag{25}$$

Recall that for the static case, the sliding velocity is replaced by the displacement jump, $[\boldsymbol{u}_\pi^v]_\tau$. We define $b_\pi^{v,k} = F_\pi^v(-\lambda_{\pi n}^{v,k} + c([\boldsymbol{u}_\pi^{v,k}]_n - g_\pi^v))$, which can be interpreted as the friction bound. The nonpenetration condition can now be rewritten as the nonlinear complementary function

$$C_n([\boldsymbol{u}_\pi^v]_n, \lambda_{\pi n}^v) = -\lambda_{\pi n}^v - \frac{1}{F_\pi^v} \max\{0, b_\pi^{v,k}\}, \tag{26}$$

where $c > 0$ is a given numerical parameter and $\max\{\cdot, \cdot\}$ is the maximum function. Similarly, we can now rewrite the Coulomb friction as the complementary function

$$\boldsymbol{C}_\tau([\dot{\boldsymbol{u}}_\pi^v], \boldsymbol{\lambda}_{\pi\tau}^v) = \max\{b_\pi^{v,k}, \|-\boldsymbol{\lambda}_{\pi\tau}^v + c[\boldsymbol{u}_\pi^v]_\tau\|\}(-\boldsymbol{\lambda}_{\pi\tau}^v) - \max\{0, b_\pi^{v,k}\}(-\boldsymbol{\lambda}_{\pi\tau}^v + c[\dot{\boldsymbol{u}}_\pi^v]_\tau). \tag{27}$$

The solution pair $(\boldsymbol{u}_\pi^v, \boldsymbol{\lambda}_\pi^v)$ satisfies the nonpenetrating condition (24) and Coulomb law (25) if and only if $C_n([\boldsymbol{u}_\pi^v]_n, \lambda_{\pi n}^v) = 0$ and $\boldsymbol{C}_\tau([\dot{\boldsymbol{u}}_\pi^v], \boldsymbol{\lambda}_\pi^v) = \boldsymbol{0}$. We apply a semismooth Newton method to this problem, which results in an active set method. Given the solution $(\boldsymbol{u}^k, \boldsymbol{\lambda}^k)$ from the previous Newton iteration, we divide the contact subfaces into three disjoint sets:

$$\begin{aligned} \mathcal{I}_n^{k+1} &= \{(\pi, v) \in \mathcal{P} : b_\pi^{v,k} \le 0\} \\ \mathcal{I}_\tau^{k+1} &= \{(\pi, v) \in \mathcal{P} : \|-\boldsymbol{\lambda}_{\pi\tau}^{v,k} + c[\dot{\boldsymbol{u}}_\pi^{v,k}]_\tau\| - b_\pi^{v,k} < 0\} \\ \mathcal{A}^{k+1} &= \{(\pi, v) \in \mathcal{P} : \|-\boldsymbol{\lambda}_{\pi\tau}^{v,k} + c[\dot{\boldsymbol{u}}_\pi^{v,k}]_\tau\| \ge b_\pi^{v,k} > 0\}. \end{aligned} \tag{28}$$

The first set contains the subfaces not in contact. The second set contains the subfaces in contact whose friction bound is not reached, i.e., they are sticking. The third set contains the subfaces in contact where the friction bound is reached, i.e., they are sliding. The new iterates $([\boldsymbol{u}_\pi^{v,k+1}]_\tau, \boldsymbol{\lambda}_{\pi\tau}^{v,k+1})$ in the semismooth Newton scheme are then calculated depending on which set the subface belongs to. The update is found by calculating the derivative of the complementary functions C_n and $\boldsymbol{C}_\tau$ for each of the three sets. For the subfaces not in contact, zero traction is enforced

$$\boldsymbol{\lambda}_\pi^{v,k+1} = \boldsymbol{0} \qquad (\pi, v) \in \mathcal{I}_n^{k+1}. \tag{29}$$

For the subfaces in contact and sticking, we enforce

$$[u_{\pi n}^{v,k+1}] = g_\pi^v, \qquad [\dot{\boldsymbol{u}}_\pi^{v,k+1}]_\tau + \frac{F_\pi^v [\dot{\boldsymbol{u}}_\pi^{v,k}]_\tau}{b_\pi^{v,k}} \lambda_{\pi n}^{v,k+1} = [\dot{\boldsymbol{u}}_\pi^{v,k}]_\tau \qquad (\pi, v) \in \mathcal{I}_\tau^{k+1}. \tag{30}$$

In the normal direction, this enforces the condition that the negative and positive subfaces must be in contact in the next iteration $k+1$. In tangential direction the enforced condition is dependent on the previous Newton iteration. If the subface sliding velocity was zero in the previous iteration, $[\dot{\boldsymbol{u}}_\pi^{v,k}] = \boldsymbol{0}$, Equation (30) enforces the condition that the tangential velocity is zero in the next iteration, $[\dot{\boldsymbol{u}}_\pi^{v,k+1}] = \boldsymbol{0}$. If the subface sliding velocity was different from zero in the previous iteration, the Newton update does not immediately enforce zero sliding velocity, however, as the algorithm converges we have $F_\pi^v \lambda_{\pi n}^{v,k+1} = b_\pi^{v,k}$, and the sliding velocity, $[\dot{\boldsymbol{u}}_\pi^k]$, for the sticking subfaces is set to zero. For subfaces in contact and sliding, we enforce

$$[\boldsymbol{u}_\pi^{v,k+1}]_n = g_\pi^v,$$
$$\boldsymbol{\lambda}_{\pi\tau}^{v,k+1} + L_\pi^{v,k}[\dot{\boldsymbol{u}}_\pi^{v,k+1}]_\tau + F_\pi^v \boldsymbol{v}_\pi^{v,k} \lambda_{\pi n}^{v,k+1} = \boldsymbol{r}_\pi^{v,k} + b_\pi^{v,k} \boldsymbol{v}_f^k, \qquad (\pi, v) \in \mathcal{A}^{k+1}. \tag{31}$$

Again, this enforces the condition that the negative and positive subfaces be in contact at the next iteration $k+1$. In the tangential direction, the condition approximates the sliding direction and distance. The matrices and vectors are:

$$L_\pi^{v,k} = c((I_{d-1} - M_\pi^{v,k})^{-1} - I_{d-1}) \tag{32}$$

$$\boldsymbol{v}_\pi^{v,k} = (I_{d-1} - M_\pi^{v,k})^{-1} \frac{-\boldsymbol{\lambda}_{\pi\tau}^{v,k} + c[\dot{\boldsymbol{u}}_\pi^{v,k}]_\tau}{\|-\boldsymbol{\lambda}_{\pi\tau}^{v,k} + c[\dot{\boldsymbol{u}}_\pi^{v,k}]_\tau\|}$$

$$\boldsymbol{r}_\pi^{v,k} = -(I_{d-1} - M_\pi^{v,k})^{-1} e_\pi^{v,k} Q_\pi^{v,k}(-\boldsymbol{\lambda}_{\pi\tau}^{v,k} + c[\dot{\boldsymbol{u}}_\pi^{v,k}]_\tau),$$

where I_{d-1} is the $(d-1 \times d-1)$ identity matrix and $M_\pi^{v,k} = e_\pi^{v,k}(I_{d-1} - Q_\pi^{v,k})$ with

$$Q_\pi^{v,k} = \frac{-\boldsymbol{\lambda}_{\pi\tau}^{v,k}(-\boldsymbol{\lambda}_{\pi\tau}^{v,k} + c[\dot{\boldsymbol{u}}_\pi^{v,k}]_\tau)^\top}{b_\pi^{v,k}\|-\boldsymbol{\lambda}_{\pi\tau}^{v,k} + c[\dot{\boldsymbol{u}}_\pi^{v,k}]_\tau\|}, \qquad e_\pi^{v,k} = \frac{b_\pi^{v,k}}{\|-\boldsymbol{\lambda}_{\pi\tau}^{v,k} + c[\dot{\boldsymbol{u}}_\pi^{v,k}]_\tau\|}.$$

Regularization

For the subfaces in the inactive set $\mathcal{I}_n^{k+1}$, i.e., the subfaces not in contact, the Newton update gives a homogeneous Neumann boundary condition. For the subfaces in the contact sets $\mathcal{I}_\tau^{k+1}$ and $\mathcal{A}^{k+1}$, the Newton update gives a Dirichlet condition in the normal direction and a Robin boundary condition in the tangential direction. This Robin condition guarantees positive definiteness of the system only if $L_\pi^{v,k}$, defined by Equation (32), is positive definite. In the converged limit, the matrix $L_\pi^{v,k}$ is a positive definite matrix[25]. However, during the iterations, there is no guarantee that this will hold. We therefore add a regularization to the Robin conditions by replacing $Q_\pi^{v,k}$ by

$$\tilde{Q}_\pi^{v,k} = \frac{-\boldsymbol{\lambda}_{\pi\tau}^{v,k}(-\boldsymbol{\lambda}_{\pi\tau}^{v,k} + c[\dot{\boldsymbol{u}}_\pi^{v,k}]_\tau)^\top}{\max(b_\pi^{v,k}, \|\boldsymbol{\lambda}_{\pi\tau}^{v,k}\|)\|-\boldsymbol{\lambda}_{\pi\tau}^{v,k} + c[\dot{\boldsymbol{u}}_\pi^{v,k}]_\tau\|},$$

which is only different from $Q_\pi^{v,k}$ when the inequalities in Equation (25) are violated. Further, we define

$$\alpha_\pi^{v,k} = \frac{(-\boldsymbol{\lambda}_{\pi\tau}^{v,k})^\top(-\boldsymbol{\lambda}_{\pi\tau}^{v,k} + c[\dot{\boldsymbol{u}}_\pi^{v,k}]_\tau)}{\|\boldsymbol{\lambda}_{\pi\tau}^{v,k}\|\|-\boldsymbol{\lambda}_{\pi\tau}^{v,k} + c[\dot{\boldsymbol{u}}_\pi^{v,k}]_\tau\|}, \qquad \delta_\pi^{v,k} = \min\left(\frac{\|\boldsymbol{\lambda}_{\pi\tau}^{v,k}\|}{\lambda_{\pi n}^{v,k}}, 1\right),$$

and

$$\beta_\pi^{v,k} = \begin{cases} \frac{1}{1 - \alpha_\pi^{v,k}\delta_\pi^{v,k}}, & \text{if } \alpha_\pi^{v,k} < 0 \\ 1, & \text{otherwise.} \end{cases}$$

Using the notation that tilde $(\tilde{\cdot})$ denotes the regularization, we have $\tilde{M}_\pi^{v,k} = e_\pi^{v,k}(I_{d-1} - \tilde{Q}_\pi^{v,k})$ and replace the matrix $L_\pi^{v,k}$ from Equation (32) by

$$\tilde{L}_\pi^{v,k} = c((I_{d-1} - \beta_\pi^{v,k}\tilde{M}_\pi^{v,k}) - I_{d-1}),$$

which guarantees its positive definiteness[25]. As the iterates $(\boldsymbol{u}^k, \boldsymbol{\lambda}^k)$ converge to the solution, the regularization $\tilde{Q}_\pi^{v,k} \to Q_\pi^{v,k}$, $\tilde{L}_\pi^{v,k} \to L_\pi^{v,k}$, and $\beta_\pi^{v,k} \to 1$, and we obtain the original system of equations.

3.3 | Discrete system of equations

We end Section 3 with a summary of the discrete system of equations that is solved at each Newton iteration, and we state the discrete linearized version of Equations (1)-(7) as:

$$
\begin{aligned}
A\boldsymbol{u} + B\boldsymbol{p} + C\boldsymbol{\lambda} &= \boldsymbol{b}_u, \\
D\boldsymbol{u} + E\boldsymbol{p} + F\boldsymbol{\lambda} &= \boldsymbol{b}_p, \\
G\boldsymbol{u} + H\boldsymbol{p} + J\boldsymbol{\lambda} &= \boldsymbol{r}.
\end{aligned}
\tag{33}
$$

The first line is the discrete momentum balance, and the matrices A, B, C, and the vector $\boldsymbol{b}_u$ are obtained by considering Equation (23) for all cells and assembling the coefficients in the global matrices. Similarly, the second row corresponds to the discrete flux balance, and the equation is obtained by considering Equation (22) over all cells and assembling the coefficients in the global matrices. The matrix F appears due to the dependence on $\boldsymbol{\lambda}$ in the local systems for the displacement gradients, as given by Equation (21). It is worth pointing out that the matrices A, B, D, and E are the same matrices as are obtained by the finite-volume scheme in a poroelastic domain without any fractures[13]. The last row of Equation (33) corresponds to the linearization of the complementary functions (26) and (27), and the matrices are obtained by assembling Equations (29)-(31) for each subface on the fracture. The dependence of the pressure in the contact law, given by the matrix H, is due to the pressure dependence on the poroelastic stress (see second row of Equation 1) as well as the pressure dependence on the displacement gradients given by Equation (21).

From a computational point of view, it is worth noting that during the Newton iteration, only the matrices G, H, J, and the vector $\boldsymbol{r}$ will change. This means that updating the discretization is inexpensive as it is only a local update for the subcells bordering the fractures.

4 | NUMERICAL EXAMPLES

Four numerical examples are given. For the first two, we neglect the fluid contribution to the mechanical stress to investigate the performance of the numerical approach for the purely mechanical contact problem, i.e., we set $\alpha = 0$. In all of the examples, Young's modulus is $E_0 = 4$ GPa, the Poisson ratio is $\nu = 0.2$, and the initial gap of the fractures is $g = 0$. In our experience, the algorithm is quite robust with respect to the numerical parameter c, and in the examples, it is fixed to $c = 100$ GPa/m.

We assign a space varying coefficient of friction so that the slip of the fractures will arrest before it reaches the fracture tips. This choice of the friction coefficient is done to obtain a solution with high enough regularity to study the convergence in stress. If the slip of the fractures reaches the fracture tips, the solution will contain singularities in the stress, which reduces the regularity of our solution. Note that our method is not restricted to the regularized solution, as discussed more thoroughly in Appendix A.

The discrete solution is denoted $\boldsymbol{u}_h$, which is interpreted as the piecewise constant function over each cell $K \ni \boldsymbol{x}$ such that $\boldsymbol{u}_h(\boldsymbol{x}) = \boldsymbol{u}_K$. The discrete solution $\boldsymbol{\lambda}_h$ for the Lagrange multiplier is defined as piecewise constant on each face π on Γ^+ and is equal to the area weighted sum of the subface values, $\boldsymbol{\lambda}_h(\boldsymbol{x})m_\pi = \sum_{v \in \mathcal{V}_\pi} m_\pi^v \boldsymbol{\lambda}_\pi^v$, $\boldsymbol{x} \in \pi$. Likewise, the displacement jump is defined as the piecewise constant on each face, π, on Γ^+ corresponding to the subface average, $[\boldsymbol{u}_h(\boldsymbol{x})] = \frac{1}{|\mathcal{V}_\pi|} \sum_{v \in \mathcal{V}_\pi} [\boldsymbol{u}_\pi^v]$, $\boldsymbol{x} \in \pi$, where $|\mathcal{V}_\pi|$ is the number of subfaces of the face, π, which is equal to three if π is a triangle. The continuous solution is denoted by the pair $(\boldsymbol{u}, \boldsymbol{\lambda})$.

We define the relative error of a discrete variable ξ_h in a domain γ as

$$
\varepsilon_\gamma(\xi_h, \xi) = \frac{\|\xi_h - \xi\|_\gamma}{\|\xi\|_\gamma},
\tag{34}
$$

where ξ is a reference solution and $\|\cdot\|_\gamma$ is the L_2 norm over the domain γ. The Newton iteration is terminated when the change in the solution is below a given stopping criterion:

$$
\varepsilon_\Omega(\boldsymbol{u}_h^{k+1}, \boldsymbol{u}_h^k) < \delta,
\tag{35}
$$

where k is the Newton iteration index.

To solve the linear system of equations at each Newton iteration, a direct solver is used if the number of degrees of freedom is less than 10 000, else, an iterative solver is used. The iterative solver uses a preconditioned GMRES iteration that is based on a Schur complement strategy, where the mechanics-fluid subsystem is approximated by a single fixed stress iteration, see [40,41] for details. Within the fixed stress iteration, the mechanics problem is solved by one AMG iteration, as implemented in [42], while a

direct solver is applied to the flow problem. In the simpler case of a pure mechanics problem, the fixed stress iteration is replaced with an AMG iteration on the mechanics subproblem.

The computer code has been implemented in the open source Python toolbox PorePy[43], which has an interface for meshing in Gmsh[44]. The run scripts for the examples are open source[45]. ParaView[46] was used to make Figures 3 and 7.
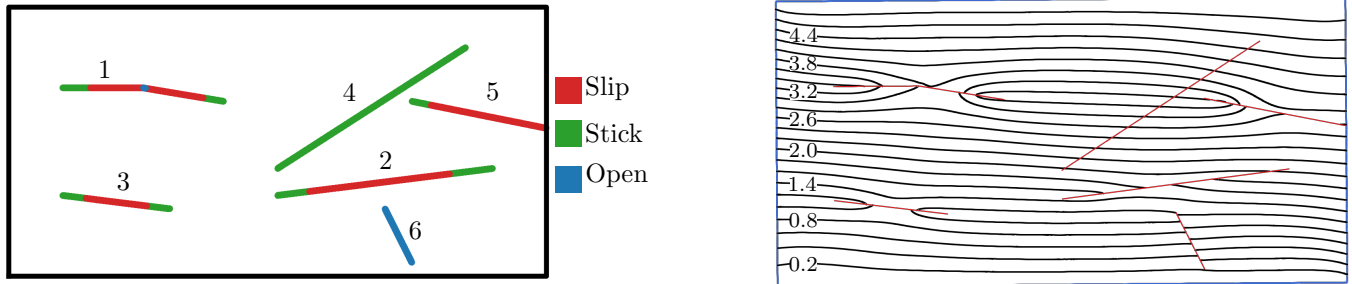

FIGURE 3 The fractured domain from Example 1. Left: The black box corresponds to the domain boundaries, while the fractures, labeled by a number, are represented by lines. The fractures are colored in three colors; segments that slip are red, segments that stick are green, and segments that open are blue. Right: Contour plot of the x-component of the displacement $\boldsymbol{u}$. The labels on the contours are given in millimeters. The red lines represent the fractures.

4.1 | Example 1

The first example is a domain 2 m × 1 m with six fractures, as depicted in Figure 3. This example includes difficult cases such as a fracture with a kink and a fracture reaching the boundary. An advantage of our finite volume method is that no special treatment is needed to handle these cases because the degrees of freedom are located in the cell and subface centers and not on the nodes. In this example, we do not consider any fluid and solve only for the linear elasticity in Equation (1) coupled to the contact conditions given in Equations (6) and (7). The bottom boundary is fixed, the two vertical boundaries are free, and at the top boundary a Dirichlet condition $\boldsymbol{g}_{u,D} = [0.005, -0.002]^{\top}$ m is assigned. The initial guess in the Newton iteration is $\boldsymbol{u} = \boldsymbol{0}$ m, $\lambda_n = -100$ Pa and $\boldsymbol{\lambda}_\tau = \boldsymbol{0}$ Pa, i.e., zero displacement and all fractures in contact and sticking. The coefficient of friction is for each fracture $i = 1 \ldots 6$ set to $F_i(\boldsymbol{x}) = 0.5(1 + \exp(-D_i(\boldsymbol{x})^2/0.005\text{m}^2)$, $\boldsymbol{x} \in \Gamma_i^+$, where $D_i(\boldsymbol{x})$ is the distance from $\boldsymbol{x}$ to the tips of fracture i. Note that the bend in Fracture 1 and the right end of Fracture 5 are not considered tips for the distance function D, and thus the coefficient of friction at these points is $F \approx 0.5$.

A contour plot of the solution is shown in Figure 3 where the discontinuous displacement over the sliding or opening fractures can clearly be seen. To better visualize the different behaviors of the fractures, the fracture regions that are slipping, sticking, and opening are plotted in different colors in Figure 3. For Fracture 1, the top boundary is sliding to the right, while the bottom boundary is sliding to the left. This situation causes the fracture to open in a small segment after the bend. Figure 4 shows the shear component of the Lagrange multiplier as well as the friction bound and displacement jump. At the bend of fracture 1, there is a singularity in the stress that causes the sharp increase in the Lagrange multiplier. For Fracture 2, we observe a change in the shear and normal component of the Lagrange multiplier at approximately the midpoint that is caused by the opening of Fracture 6. In the vicinity of the fracture tips, there is a sharp increase in the shear component of the Lagrange multiplier as the fractures change behavior from sliding to sticking.

As a reference solution $(\boldsymbol{u}, \boldsymbol{\lambda})$, we use the solution calculated for a fine mesh using 1.7 million degrees of freedom. The second finest mesh has 270 thousand degrees of freedom and is the mesh used for the results in Figure 4 and 3 . In Figure 5, the relative errors $\varepsilon_{\Gamma_i^+}([\boldsymbol{u}_h], [\boldsymbol{u}])$ and $\varepsilon_{\Gamma_i^+}(\boldsymbol{\lambda}_h, \boldsymbol{\lambda})$, given by Equation (34), are plotted for each fracture $i = 1, \ldots, 6$. For the displacement jump, the convergence is of first-order for all fractures except Fracture 4, which is correctly predicted to be sticking (and thus, the error is zero). For the Lagrange multiplier $\boldsymbol{\lambda}_h$, we observe first-order convergence for Fractures 4 and 5, while the error for Fracture 6 is zero. The convergence rates for traction is typically observed to be of first-order in the L_2 norm and second-order in the 2-norm for the finite-volume scheme[12,13], but the Lagrange multiplier for fractures 1, 2 and 3 shows somewhat lower convergence rates than first-order. However, this is not surprising due to the low regularity of the Lagrange multipliers. Figure 6 shows first-order convergence of the error for the discrete displacement $\boldsymbol{u}_h$ in the 2d domain Ω. Finally, Table 2 shows that the number of Newton iterations do not grow significantly when the mesh is refined.
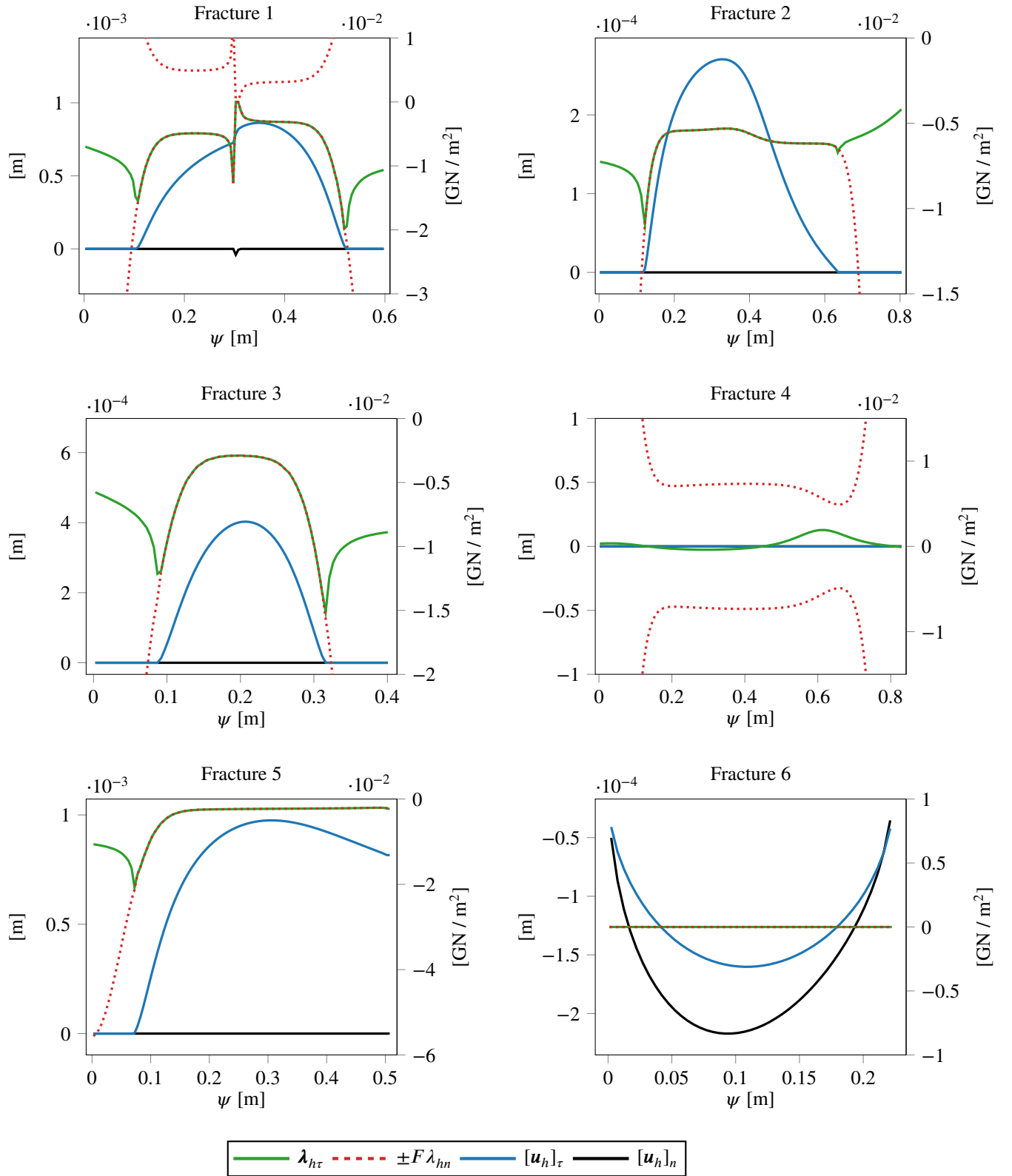
FIGURE 4 Results from Example 1 showing $\boldsymbol{\lambda}_h$ and $[\boldsymbol{u}_h]$ for the reference solution that has an average of 103 faces along each fracture. The shear component of the Lagrange multiplier $\boldsymbol{\lambda}_{h\tau}$ (green), friction bound $\pm F \boldsymbol{\lambda}_{hn}$ (red dashes), tangential displacement jump $[\boldsymbol{u}_h]_\tau$ (blue), and normal displacement jump $[\boldsymbol{u}_h]_n$ (black) for all fractures. The x-axis shows the distance ψ from the leftmost end of the fracture. The subplots are arranged from top left to bottom right according to the fracture number given in Figure 3.
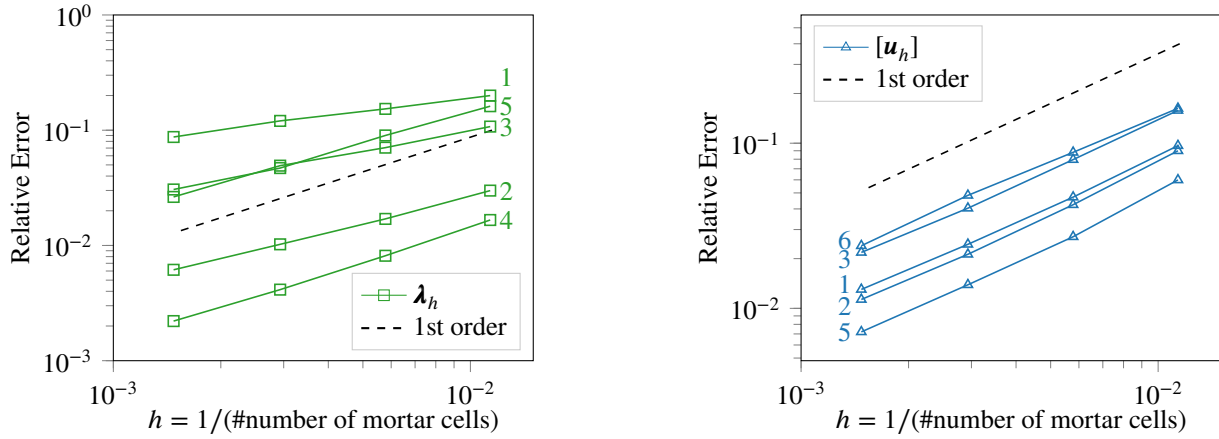
FIGURE 5 Convergence rates for the Lagrange multiplier $\boldsymbol{\lambda}_h$ (left) and the displacement jump $[\boldsymbol{u}_h]$ (right) for each separate fracture in Example 1. The error is measured as the relative errors $\varepsilon_{\Gamma_i^+}([\boldsymbol{u}_h], [\boldsymbol{u}])$ and $\varepsilon_{\Gamma_i^+}(\boldsymbol{\lambda}_h, \boldsymbol{\lambda})$ for each fracture Γ_i^+. The line numbering corresponds to the fracture numbers given in Figure 3.
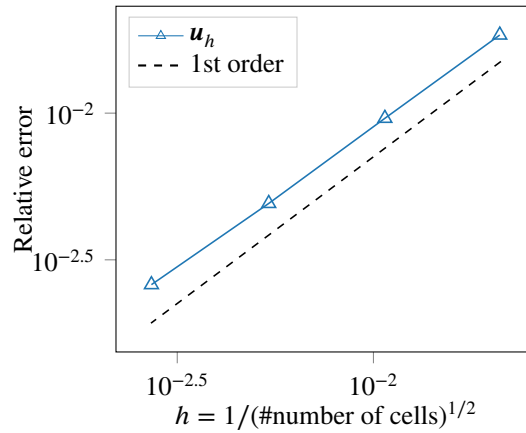
FIGURE 6 Convergence rates for the cell-centered displacement in Example 1. The error is the relative error $\varepsilon_\Omega(\boldsymbol{u}_h, \boldsymbol{u})$, as defined by Equation (34).

4.2 | Example 2

In this example Ω is a 3d domain $(-200, 300) \times (-200, 300) \times (-300, 300)$ m with two circular fractures approximated by polygons with 10 vertices. The location and geometry of the fractures are given in Table 1. As in the previous example, no fluid is included. The bottom boundary is fixed, the four vertical boundaries are rolling, and at the top boundary, a load is applied downwards by enforcing a Neumann condition $\boldsymbol{g}_{u,N} = [0, 0, -4.5]^\top$ MPa. The coefficient of friction is for the two fractures, $i = 1, 2$:

$$F_i(\boldsymbol{x}) = 0.5 \exp\left(\frac{10\text{m}}{R_i - D_i(\boldsymbol{x})} - \frac{10\text{m}}{R_i}\right),$$

where R_i is the radius of fracture i and $D_i(\boldsymbol{x})$ the distance from the center of the fracture to $\boldsymbol{x}$.

Figure 7 shows the displacement jump $[\boldsymbol{u}_h]_\tau$ and the shear component of the Lagrange multiplier $\boldsymbol{\lambda}_{h\tau}$. The fractures are in contact, i.e., the normal displacement jump $[\boldsymbol{u}_h]_n = 0$ is zero. Going from two dimensions to three adds an additional challenge to the contact problem as we have to find not only the magnitude of the slip but also the direction. The advantage of the hybrid formulation in combination with a semismooth Newton scheme is that the same computer code can be used for any dimension, and as observed in the figure, the correct sliding direction (parallel to the Lagrange multiplier) is found by the algorithm.

The errors are calculated by comparison to a reference solution that has 500 thousand degrees of freedom. The relative errors $\varepsilon_{\Gamma_i^+}([\boldsymbol{u}_h], [\boldsymbol{u}])$ and $\varepsilon_{\Gamma_i^+}(\boldsymbol{\lambda}_h, \boldsymbol{\lambda})$ for the two fractures, $i = 1, 2$, are shown in Figure 8. We observe first-order convergence for the

TABLE 1 Fracture geometry in Example 2 and 3. The strike angle is the rotation from x-axis in the x-y-plane defining the strike line. The dip angle is rotation around the strike line.

	Fracture 1	Fracture 2
Center	$-[10, 30, 80]^\top$ m	$[15, 60, 80]^\top$ m
Radius	150 m	150 m
Strike angle	81.8°	78.3°
Dip angle	43.9°	47.1°
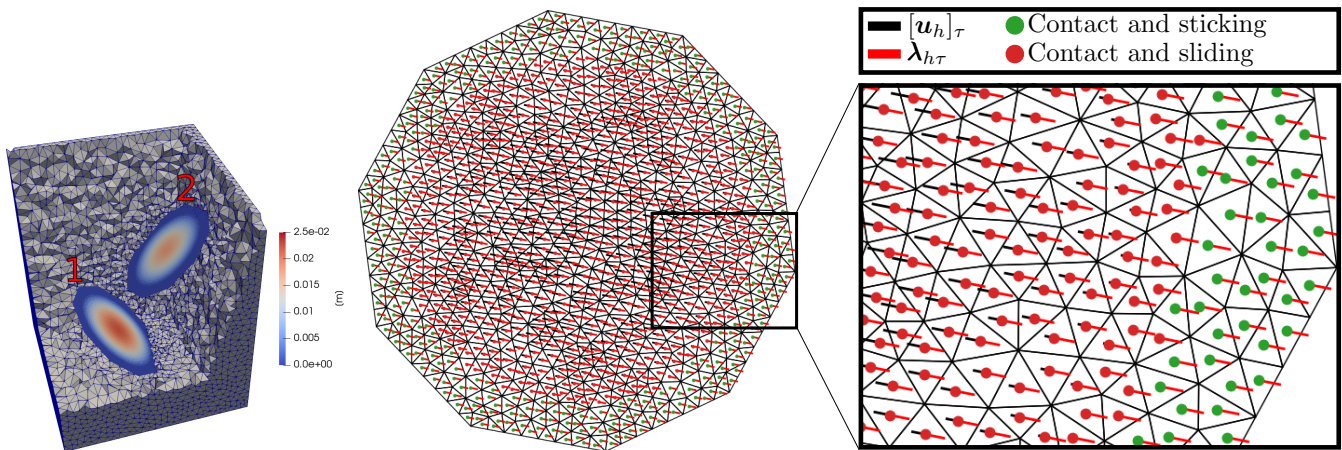
FIGURE 7 Results from Example 2 using approximately 250 thousand degrees of freedom. Left: Displacement jump $\|[u_h]\|$ for the two fractures indicated by the fracture number. Parts of the 3d mesh are cropped to reveal the fractures. Middle: The surface mesh of Γ^+ of Fracture 1. The red lines show the tangential part of the Lagrange multiplier $\lambda_{h\tau}$ while the black lines show the scaled displacement jumps $400[u_h]_\tau$. Right: Zoomed view of middle figure.

displacement jump, while the Lagrange multiplier shows a somewhat reduced order of convergence. Finally, Table 2 shows the number of Newton iterations for each mesh, and we do not observe any significant increase in the number of Newton iterations as the mesh is refined.

TABLE 2 The number of Newton iterations used for the different mesh sizes in Example 1 and 2. The number of fracture faces and number of cells are given in the table.

	Example 1			Example 2	
# fracture faces	# cells	# iterations	# fracture faces	# cells	# iterations
176	4538	5	126	449	3
346	17482	4	450	1878	3
682	68330	5	1884	11825	3
1356	270756	7	7728	160417	4

4.3 | Example 3

In this example, we consider the same domain and material parameters as in Example 1, but add a fluid. The permeability of the fluid is $\mathcal{K} = 10^{-8}$ m²Pa⁻¹s⁻¹, the storage coefficient is $c_0 = 1 \cdot 10^{-10}$ Pa⁻¹, and the Biot coefficient is $\alpha = 1$. The initial
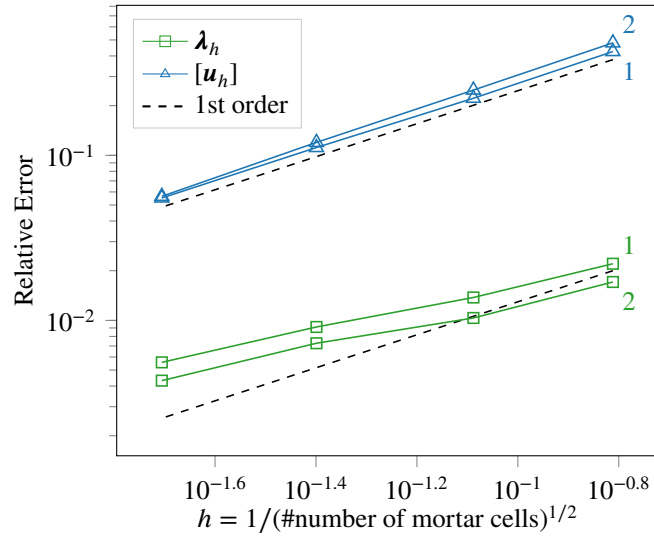
FIGURE 8 Convergence rates for the two fractures in Example 2. The error is measured as the relative errors, $\varepsilon_{\Gamma_i^+}([\boldsymbol{u}_h], [\boldsymbol{u}])$ and $\varepsilon_{\Gamma_i^+}(\boldsymbol{\lambda}_h, \boldsymbol{\lambda})$, for each fracture, Γ_i^+, as given in Equation 34. The numbering of the lines correspond to the fracture number.

displacement and pressure is set to zero, and the end time of the simulation is set to $T = 5c_0 H^2 / \mathcal{K}$, where $H = 1$ m is the height of the domain. For the fluid, we enforce homogeneous Neumann conditions on all sides except the left boundary, where a zero pressure condition is given. For the mechanics, the left and the right boundaries are given a homogeneous Neumann condition, and the bottom boundary is given a zero Dirichlet condition. The top boundary is given a time varying boundary condition given by

$$g_{u,D}(\boldsymbol{x}, t) = \begin{cases} [0.005 \text{ m}, -0.002 \text{ m}]^\top 2t/T, & t < T/2 \\ [0.005 \text{ m}, -0.002 \text{ m}]^\top, & t \geq T \end{cases} \quad \boldsymbol{x} \text{ on top boundary.}$$

This condition enforces a linear increase of the boundary condition values in the first half of the simulation, and after the boundary condition reaches the same value as in Example 1 we keep it constant for the remainder of the simulation.
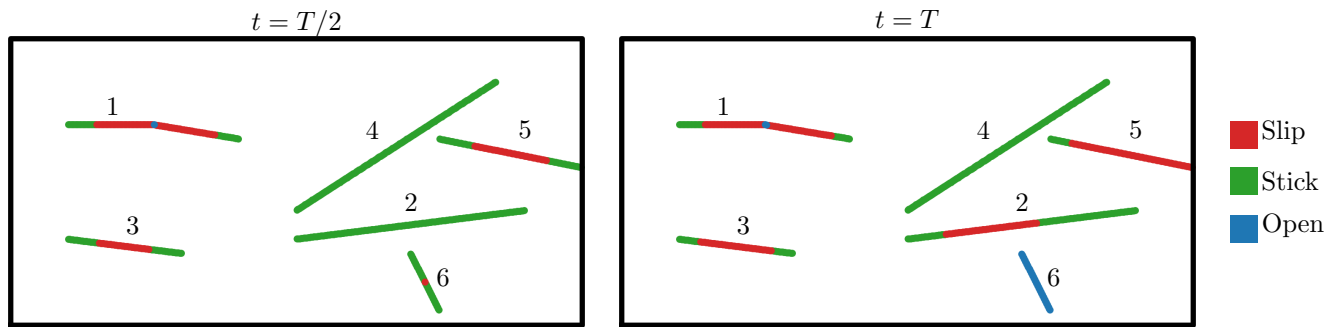

FIGURE 9 The fractured domain from Example 3. The black box corresponds to the domain boundaries, while the fractures, labeled by a number, are represented by lines. The fractures are colored in three colors; segments that slip are red, segments that stick are green, and segments that open are blue. The left figure shows the deformation half-way through the simulation, while the right figure, shows the deformation at the end time of the simulation.

In the first half of the simulation, the domain is compressed and the fluid pressure in the domain increases. In Figure 9, we plot the regions of the fractures that slip, stick and open for the two times $t = T/2$ and $t = T$. At the time $t = T/2$, the boundary condition for the mechanics is the same as in Example 1, however, we see considerable differences in the fracture displacement (compared to Figure 3) that are due to the introduction of the fluid. After $t = T/2$ the displacement boundary condition is fixed at
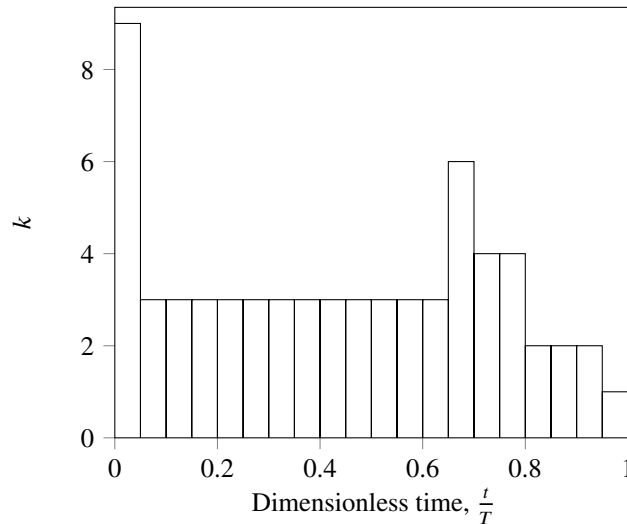
FIGURE 10 The number of Newton iterations at each time step for the simulation in Example 3.

$[0.005, -0.002]^{\top}$ m, and the fluid pressure decrease due to the zero pressure condition on the left boundary. This causes further deformation of the fractures, and at the end of the simulation the pressure in the whole domain is relatively close to zero, and the solution is approximately equal the solution in Example 1.

The number of Newton iterations for each time step is shown in Figure 10. For most iterations, the Newton solver converges in three iterations. The increase in the number of iterations needed at time $t/T = 0.65$ is believed to be related to Fracture 6 changing behavior from sliding to opening. At the end of the simulation the system is close to steady state, and the Newton solver converges in one iteration.

4.4 | Example 4

In this example, the same setup as in Example 2 is used, but a fluid is included. The domain is sealed for the fluid, i.e., homogeneous Neumann conditions, for all sides except the top boundary, which is given a Dirichlet condition $g_{p,D} = 0$ Pa. The permeability is $\mathcal{K} = 10^{-8}$ m^{2}Pa^{-1}s^{-1}, the storage coefficient $c_0 = 1 \cdot 10^{-10}$ Pa^{-1}, and the Biot coefficient $\alpha = 1$. The initial displacement and pressure is set to zero.

Without the fractures, this setup is equivalent to a consolidation problem, which can be found in standard textbooks[47]. When the load is applied to the top surface at time $t = 0$, there is an instantaneous increase in the pore pressure in the domain. The fluid will then drain slowly out from the top surface and finally relax back to the initial condition. As this process occurs, the domain will continue to deform vertically increasing the mechanical load on the fractures, which causes them to slip. Twenty time steps are taken, and the simulation is stopped after 625 minutes, at which time, for practical purposes, equilibrium is reached.

The slip over time is plotted in Figure 11. Initially, the pore pressure carries most of the applied load, and the fractures are not sliding. As the fluid drains and the domain deforms, the tangential part of the Lagrange multiplier on the fractures increases, and after approximately 150 minutes, the fractures start to slide. The sliding then gradually slows down and qualitatively reaches the solution of the drained medium, i.e., the solution from Example 2. There are small differences between the solution from this example at the final time and the solution of Example 2, which are caused by the use of a dynamic friction model in this example and a static friction model in Example 2.

The number of iterations needed for convergence of the Newton solver at each time step is shown in Figure 11. For the first time step, 6 Newton iterations are needed, which is twice as many as for any of the other time steps. It is well known that the Newton strategy is very sensitive to the initial guess. A naive choice generally results in an increase in the required number of Newton iterations for smaller mesh sizes. However, either in a dynamic or a multilevel context, there are good options to set the initial guess[25,20]. In this case, the initial condition at $t = 0$ is ($\boldsymbol{\lambda} = \boldsymbol{0}$ and $\boldsymbol{u} = \boldsymbol{0}$), which assigns all subfaces to the noncontact set, $\mathcal{I}_n$, while those at the first time step belong to the sticking set $\mathcal{I}_\tau$ (see Equation (28)). During the dynamic sliding, the initial guess (the solution from the previous time step) gives a good approximation of the solution in the current time step, and thus,
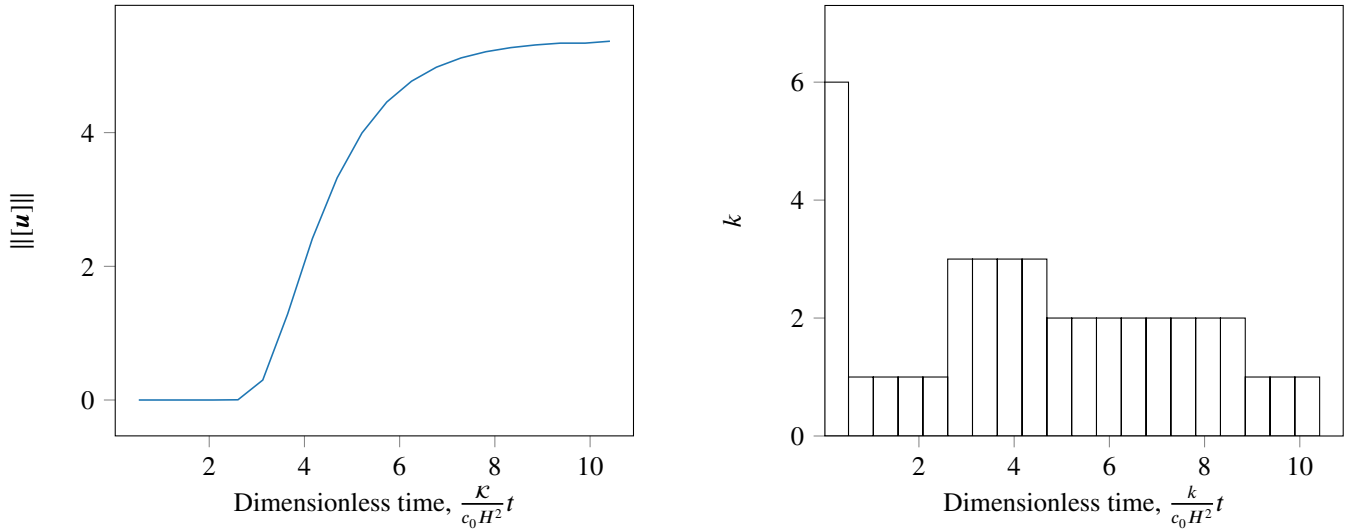
FIGURE 11 Results from Example 4. The length scale $H = 600$ m is the height of the domain. Left: Slip distance as a function of time. Right: Convergence of the Newton solver. Each time step is represented by a rectangle, and the *y*-axis shows the number of Newton iterations needed until the convergence tolerance is reached.

fewer iterations are needed. As the fractures start to slide at time step six, a few Newton iterations are needed for convergence. However, when approaching steady state, the algorithm predicts the correct slip in just one iteration.

5 | CONCLUSION

In this paper, we present an approach for solving the poroelastic Biot equations in a fractured domain. A classical hybrid formulation for contact mechanics is combined with a finite volume discretization for poroelasticity. The fractures are modeled as internal contact boundaries and are governed by a nonpenetration condition in the normal direction and a Coulomb friction law in the tangential direction. The inequalities in the contact conditions are handled by a semismooth Newton method. The finite volume discretization has several advantages for these types of problems. The cell-center colocation of the discrete displacement and pressure variables gives a sparse linear system, efficient data structures, and no need for staggered grids. Moreover, the contact conditions are obtained naturally in the discretization as a condition per subface in the local systems. Thus, these conditions can be treated in an equivalent manner to boundary conditions on the external boundary. Finally, there is no need for special treatment of the contact conditions in the poroelastic case versus the purely elastic case, as the correct pressure contribution to the effective stress is obtained in the local system.

We showed that the hybrid formulation coupled with the finite volume discretization handles a given spatially varying coefficient of friction. The formulation is also suitable for other friction models such as rate and state friction or temperature-dependent coefficient of friction.

Four numerical examples illustrate the method's robustness and applicability to difficult cases. By comparison to a reference solution, the discrete solution shows first-order convergence in displacements and slightly less than first-order convergence for the Lagrange multipliers. We also show that the method handles singularity in the solution resulting from a piecewise linear fracture with a kink. Finally, a 3d example is presented where we study the effect of the fluid pressure on the solution.

The model presented in this work is limited to fluid flow in the matrix. A natural extension is to include fluid flow also in the fractures. The fluid pressure in the fracture will then act as a force on the fracture sides, effectively reducing the normal traction. Experiments have also shown that asperities along fracture surfaces can have a very important effect on both the opening and sliding of fractures. These effects can be included by adding a nonlinear deformation model to the fractures. The advantage of our framework is that any nonlinear extensions to the model can be included in the same Newton iteration, which might be crucial for the convergence of the resulting scheme.

References

1. Coussy O. *Poromechanics*. Wiley . 2003.

2. Bear J. *Dynamics of Fluids in Porous Media*. Dover Civil and Mechanical Engineering SeriesDover . 1988.

3. Russell TF. Relationships among Some Conservative Discretization Methods. In: Chen Z, Ewing RE, Shi ZC. , eds. *Numerical Treatment of Multiphase Flows in Porous Media*Springer Berlin Heidelberg; 2000; Berlin, Heidelberg: 267–282.

4. Raviart PA, Thomas JM. A mixed finite element method for 2-nd order elliptic problems. In: Galligani I, Magenes E., eds. *Mathematical Aspects of Finite Element Methods*Springer Berlin Heidelberg; 1977; Berlin, Heidelberg: 292–315.

5. Cai Z, Jones J, McCormick S, Russell T. Control-volume mixed finite element methods. *Computational Geosciences* 1997; 1(3): 289–315. doi: 10.1023/A:1011577530905

6. Aavatsmark I. An Introduction to Multipoint Flux Approximations for Quadrilateral Grids. *Computational Geosciences* 2002; 6(3): 405–432. doi: 10.1023/A:1021291114475

7. Vermeer PA, Verruijt A. An accuracy condition for consolidation by finite elements. *International Journal for Numerical and Analytical Methods in Geomechanics* 1981; 5(1): 1-14. doi: 10.1002/nag.1610050103

8. Haga JB, Osnes H, Langtangen HP. On the causes of pressure oscillations in low-permeable and low-compressible porous media. *International Journal for Numerical and Analytical Methods in Geomechanics* 2012; 36(12): 1507-1522. doi: 10.1002/nag.1062

9. Murad MA, Loula AFD. On stability and convergence of finite element approximations of Biot's consolidation problem. *International Journal for Numerical Methods in Engineering* 1994; 37(4): 645-667. doi: 10.1002/nme.1620370407

10. Aguilar G, Gaspar F, Lisbona F, Rodrigo C. Numerical stabilization of Biot's consolidation model by a perturbation on the flow equation. *International Journal for Numerical Methods in Engineering* 2008; 75(11): 1282-1300. doi: 10.1002/nme.2295

11. Nordbotten JM. Cell-centered finite volume discretizations for deformable porous media. *International Journal for Numerical Methods in Engineering* 2014; 100(6): 399-418. doi: 10.1002/nme.4734

12. Keilegavlen E, Nordbotten JM. Finite volume methods for elasticity with weak symmetry. *International Journal for Numerical Methods in Engineering* 2017; 112(8): 939–962. doi: 10.1002/nme.5538

13. Nordbotten J. Stable Cell-Centered Finite Volume Discretization for Biot Equations. *SIAM Journal on Numerical Analysis* 2016; 54(2): 942-968. doi: 10.1137/15M1014280

14. Kikuchi N, Oden J. *Contact problems in elasticity: A study of variational inequalities and finite element methods*. SIAM studies in applied mathematics 8 . 1988.

15. Wriggers P. *Computational Contact Mechanics*. Springer, Berlin, Heidelberg. 2 ed. 2006

16. Kikuchi N, Joon Song Y. Penalty/finite-element approximation of a class of unilateral problems in linear elasticity. *Quarterly of Applied Mathematics* 1981; 39. doi: 10.1090/qam/613950

17. Ben Belgacem F, Renard Y. Hybrid finite element methods for the Signorini problem. *Math. Comput.* 2003; 72: 1117-1145.

18. McDevitt TW, Laursen TA. A mortar-finite element formulation for frictional contact problems. *International Journal for Numerical Methods in Engineering* 2000; 48(10): 1525-1547. doi: 10.1002/1097-0207(20000810)48:10<1525::AID-NME953>3.0.CO;2-Y

19. Puso MA, Laursen TA. A mortar segment-to-segment frictional contact method for large deformations. *Computer Methods in Applied Mechanics and Engineering* 2004; 193(45): 4891 - 4913. doi: 10.1016/j.cma.2004.06.001

20. Wohlmuth B. Variationally consistent discretization schemes and numerical algorithms for contact problems. *Acta Numerica* 2011; 20: 569-734. doi: 10.1017/S0962492911000079

21. Moinfar A, Sepehrnoori K, Johns RT, Varavei A. Coupled Geomechanics and Flow Simulation for an Embedded Discrete Fracture Model. *SPE Reservoir Simulation Symposium* 2013. doi: 10.2118/163666-MS

22. Mikelić A, Wheeler MF, Wick T. Phase-field modeling of a fluid-driven fracture in a poroelastic medium. *Computational Geosciences* 2015; 19(6): 1171–1195. doi: 10.1007/s10596-015-9532-5

23. Giovanardi B, Formaggia L, Scotti A, Zunino P. Unfitted FEM for Modelling the Interaction of Multiple Fractures in a Poroelastic Medium. In: Bordas SPA, Burman E, Larson MG, Olshanskii MA., eds. *Geometrically Unfitted Finite Element Methods and Applications*. Springer International Publishing; 2017; Cham: 331–352.

24. Garipov TT, Karimi-Fard M, Tchelepi HA. Discrete fracture model for coupled flow and geomechanics. *Computational Geosciences* 2016; 20(1): 149–160. doi: 10.1007/s10596-015-9554-z

25. Hüeber S, Stadler G, Wohlmuth B. A Primal-Dual Active Set Algorithm for Three-Dimensional Contact Problems with Coulomb Friction. *SIAM Journal on Scientific Computing* 2008; 30(2): 572-596. doi: 10.1137/060671061

26. Bernardi C, Maday Y, Patera AT. A new nonconforming approach to domain decomposition: The mortar element method. In: Brezis H, Lions JL. , eds. *Nonlinear Partial Differential Equations and their Applications*. XI of *Collège de France Seminar*. 1994 (pp. 13–51).

27. Ucar E, Keilegavlen E, Berre I, Nordbotten JM. A finite-volume discretization for deformation of fractured media. *Computational Geosciences* 2018; 22(4): 993–1007. doi: 10.1007/s10596-018-9734-8

28. Ucar E, Berre I, Keilegavlen E. Postinjection Normal Closure of Fractures as a Mechanism for Induced Seismicity. *Geophysical Research Letters* 2017; 44(19): 9598-9606. doi: 10.1002/2017GL074282

29. Berge RL, Berre I, Keilegavlen E. Reactivation of Fractures in Subsurface Reservoirs—A Numerical Approach Using a Static-Dynamic Friction Model. In: Radu FA, Kumar K, Berre I, Nordbotten JM, Pop IS., eds. *Numerical Mathematics and Advanced Applications ENUMATH 2017*. Springer International Publishing; 2019; Cham: 653–660.

30. Hüeber S. *Discretization techniques and efficient algorithms for contact problems*. PhD thesis. Universität Stuttgart, Stuttgart; 2008.

31. Biot MA. General Theory of Three-Dimensional Consolidation. *Journal of Applied Physics* 1941; 12(2): 155-164. doi: 10.1063/1.1712886

32. Dietrich P, Helmig R, Sauter M, Hötzl H, Köngeter J, Teutsch G. *Flow and Transport in Fractured Porous Media*. Springer, Berlin, Heidelberg . 2005

33. Ucar E, Berre I, Keilegavlen E. Three-Dimensional Numerical Modeling of Shear Stimulation of Fractured Reservoirs. *Journal of Geophysical Research: Solid Earth* 2018; 123(5): 3891–3908. doi: 10.1029/2017JB015241

34. Martin V, Jaffré J, Roberts J. Modeling Fractures and Barriers as Interfaces for Flow in Porous Media. *SIAM Journal on Scientific Computing* 2005; 26(5): 1667–1691. doi: 10.1137/S1064827503429363

35. D´Angelo C, Scotti A. A mixed finite element method for Darcy flow in fractured porous media with non-matching grids. *ESAIM: M2AN* 2012; 46(2): 465–489. doi: 10.1051/m2an/2011148

36. Eymard R, Gallouët T, Herbin R. Finite Volume Methods. *Update from Handbook of Numerical Analysis* 2003; 7: 713–1020. Accessed online 4. Apr. 2019: https://old.i2m.univ-amu.fr/ herbin/PUBLI/bookevol.pdfa.

37. Klausen RA, Radu FA, Eigestad GT. Convergence of MPFA on triangulations and for Richards' equation. *International Journal for Numerical Methods in Fluids* 2008; 58(12): 1327–1351. doi: 10.1002/fld.1787

38. Friis H, Edwards M, Mykkeltveit J. Symmetric Positive Definite Flux-Continuous Full-Tensor Finite-Volume Schemes on Unstructured Cell-Centered Triangular Grids. *SIAM Journal on Scientific Computing* 2009; 31(2): 1192–1220. doi: 10.1137/070692182

39. Gaspar FJ, Lisbona FJ, Oosterlee CW. A stabilized difference scheme for deformable porous media and its numerical resolution by multigrid methods. *Computing and Visualization in Science* 2008; 11(2): 67–76. doi: 10.1007/s00791-007-0061-1

40. Kim J, Tchelepi H, Juanes R. Stability and convergence of sequential methods for coupled flow and geomechanics: Fixed-stress and fixed-strain splits. *Computer Methods in Applied Mechanics and Engineering* 2011; 200(13): 1591–1606. doi: 10.1016/j.cma.2010.12.022

41. Both JW, Borregales M, Nordbotten JM, Kumar K, Radu FA. Robust fixed stress splitting for BiotâĂŹs equations in heterogeneous media. *Applied Mathematics Letters* 2017; 68: 101–108. doi: 10.1016/j.aml.2016.12.019

42. Olson LN, Schroder JB. PyAMG: Algebraic Multigrid Solvers in Python v4.0. https://github.com/pyamg/pyamg; 2018. Release 4.0.

43. Keilegavlen E, Fumagalli A, Berge R, Stefansson I, Berre I. PorePy: An Open-Source Simulation Tool for Flow and Transport in Deformable Fractured Rocks. *arXiv* 2017. arXiv:1712.00460.

44. Geuzaine C, Remacle JF. Gmsh: A 3-D finite element mesh generator with built-in pre- and post-processing facilities. *International Journal for Numerical Methods in Engineering* 2009; 79(11): 1309-1331. doi: 10.1002/nme.2579

45. Berge RL, Keilegavlen E. Finite volume discretization for poroelastic media with fractures modeled by contact mechanics: Code. Zenodo; 2019. doi: 10.5281/zenodo.3371373

46. Ayachit U. *The ParaView Guide: A Parallel Visualization Application*. USA: Kitware, Inc. . 2015.

47. Jaeger J, Cook N, Zimmerman R. *Fundamentals of rock mechanics*. Wiley-Blackwell. 4 ed. 2007.

48. Lazzarin P, Tovo R. A unified approach to the evaluation of linear elastic stress fields in the neighborhood of cracks and notches. *International Journal of Fracture* 1996; 78(1): 3–19. doi: 10.1007/BF00018497

☐

APPENDIX

A

When a fracture slides or opens, the linear elastic stress will contain a singularity at the fracture tips[48], which causes challenges for any numerical method. We illustrate this in Figure A1, where we plot the typical stress and displacement profiles for a sliding fracture and a constant friction coefficient $F = 0.5$. We observe small oscillations in the Lagrange multiplier around the tips of the fracture. The issue is that as we approach the fracture tips, an infinitesimal change in the displacement jump will induce an infinite change in the stress. These oscillations are reflected in the errors plotted in Figure A2, where the error rate for the Lagrange multiplier deteriorates. Convergence is not seen in the Lagrange multiplier. Because the face traction values away from the fracture tips are almost constant, the error in this region is very small, and thus, the error in the Lagrange multiplier is completely dominated by the oscillations near the tips. Note that the convergence rates for the displacement jump is of order 1, as expected. To study the convergence of the Lagrange multiplier, we can regularize the solution by increasing the friction bound smoothly in a small region around the tips. In this example, this is done by setting

$$F(\boldsymbol{x}) = 0.5(1 + 10 \exp(-800 \text{ m}^{-2} D(\boldsymbol{x})^2)) \qquad \boldsymbol{x} \in \Gamma^+,$$

where $D(\boldsymbol{x})$ is the distance from $\boldsymbol{x}$ to the tips of the fracture. As seen in Figure A1, this arrests the fracture before the tip, and the added regularity gives first-order convergence in both the Lagrange multiplier and displacements, as shown in Figure A2.

The worst oscillations that we have encountered in 3d using our finite volume scheme coupled with the hybrid formulation are shown in Figure A3. The setup in this example is the same as the setup in Section 4.2 but with only Fracture 1 and a constant coefficient of friction, $F = 0.5$. Thus, we have sliding reaching the tip of the fractures. The oscillations have an amplitude
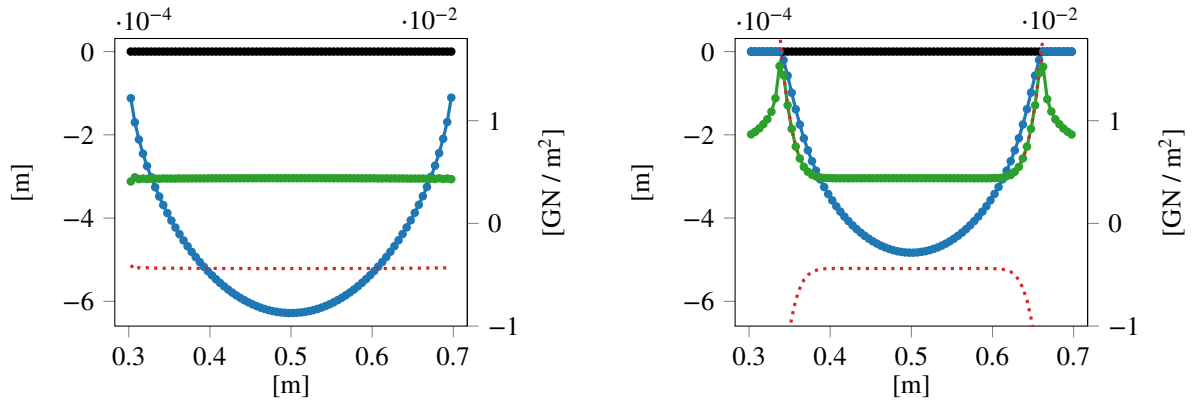
FIGURE A1 The shear component λ_τ (green), friction bound $\pm F\lambda_n$ (red dashes), tangential displacement jump $[\boldsymbol{u}]_\tau$ (blue), and normal displacement jump $[\boldsymbol{u}]_n$ (black) for the fracture. The dots correspond to the face-centered values. Left: Constant friction coefficient. Right: Regularized coefficient.
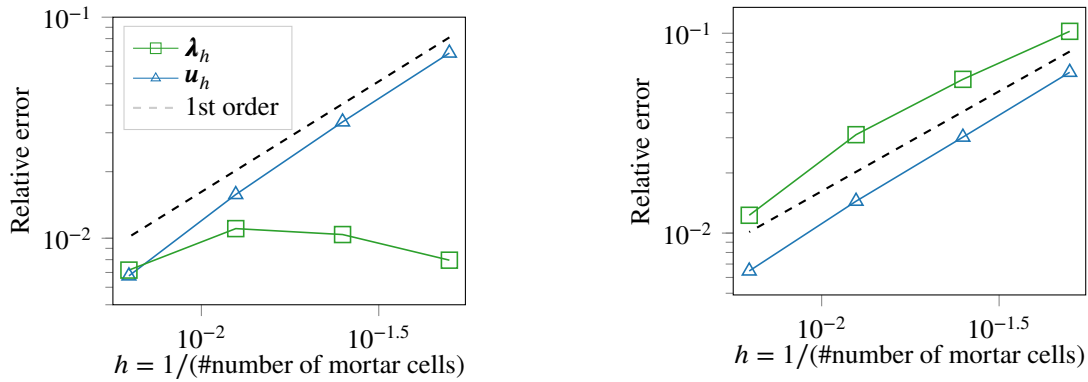

FIGURE A2 Convergence rates for the jump $[\boldsymbol{u}_h]$ and Lagrange multiplier λ_h on Γ^+. The y-axis shows the relative error $\|\boldsymbol{v}_h - \boldsymbol{v}\|_{\Gamma^+}/\|\boldsymbol{v}\|_{\Gamma^+}$, $\boldsymbol{v} \in \{[\boldsymbol{u}], \boldsymbol{\lambda}\}$. Left: The convergence of the unregularized solution. Right: The convergence of the regularized solution.

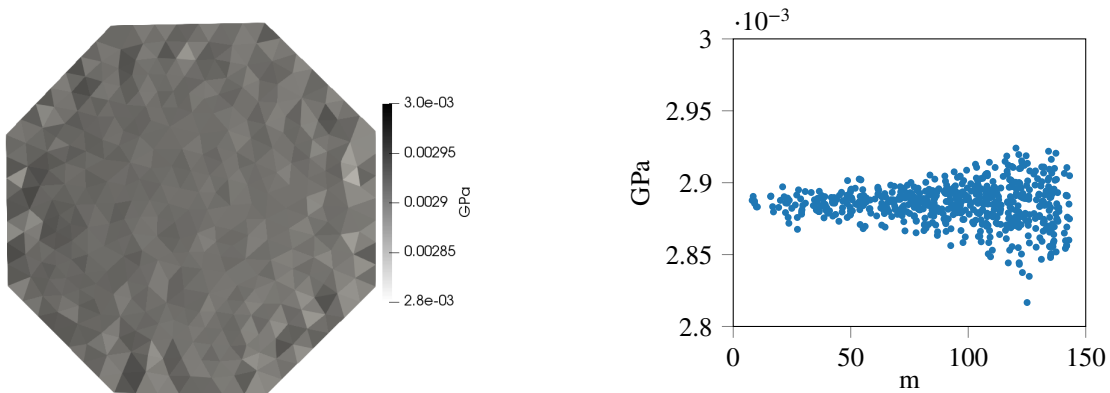**FIGURE A3** Oscillations in the normal component of the Lagrange multiplier. Left: The negative normal component of the Lagrange multiplier $-\boldsymbol{\lambda}$ on the fracture. Right: The negative normal component of the Lagrange multiplier $-\boldsymbol{\lambda}$, where the x-axis is the radial distance from the fracture center, i.e., the center is at $x = 0$, while the tip is at $x \approx 150$ m..

of approximately 5 percent from the mean traction and grow larger as we approach the fracture tips. As in the 2d case, the displacement jump $[\boldsymbol{u}_h]$ is not effected significantly by these oscillations.

Note that the singularity at the fracture tips is a challenge for any numerical method. Similar oscillations for first- and second-order Galerkin finite elements are reported, for example, by Garipov et al [24, Fig. 8], for a setup where they study a single sliding fracture.